PCCP

ROYAL SOCIETY OF CHEMISTRY

PAPER

View Article Online
View Journal | View Issue

Cite this: *Phys. Chem. Chem. Phys.*, 2024, **26**, 13973

Bubble-assisted microstreaming during electrode deposition of Mn_2O_3 energy harvesters†

Sanchia Mae Kharphanbuh, [a] Prahlad K. Baruah, [b] Alika Khare [c] and Arpita Nath *[a]

Received 6th December 2023,
Accepted 17th April 2024

DOI: 10.1039/d3cp05939a

rsc.li/pccp

The deposition of energy-harvesting Mn_2O_3 onto the "Cu" electrode is reported using pulsed laser ablation at the manganese–water interface. Conventionally, laser-induced plasma deposition is carried out by orthogonally placing the substrate (electrodes) in the plasma expansion. Here, underwater material deposition is observed on electrodes placed parallel to the plasma expansion. The possible role played by the fluid dynamically assisted microbubbles in transporting the materials onto electrodes is investigated here. To verify the influence of microbubbles, external electric fields are employed, and implications for the electrodes are characterized. The studies reveal that the external field intensifies the flow of the microbubbles towards the walls, which assists in the deposition of Mn_2O_3 on the electrodes.

1. Introduction

Pulsed laser ablation in liquid (PLAL) with a submerged solid target uses a powerful laser beam that, upon irradiation, ablates the target surface and forms a hot plasma that adiabatically expands against the liquid medium. Due to the suppression of plasma expansion by the surrounding liquid, it forcefully ejects its constituent species into the liquid medium that acts as a nucleation site for the formation of nanoparticles. Later, in these active sites, nanoparticles are surrounded by micrometer-sized bubbles, reportedly known as persistent microbubbles, child bubbles, or microscopic bubbles.[1–4] In addition, a concurrent vapor layer of a macro bubble (diameter a few mm) encasing the transient plasma is observed at the target–liquid interface.[2] Following plasma cooling, the remnant nanoparticles are formed inside macro bubbles, oscillating to maintain the surrounding liquid hydrostatic pressure. These nanoparticles are dispersed in the liquid predominantly during the collapse phase.[5]

Numerous reports are available on transient cavitation (macro) bubbles, with more recent work focusing on persistent (micro)bubbles.[6–9] The microbubbles exhibit a large specific surface area, a higher mass transfer coefficient, slow rising velocity, and larger free radicals, finding implications in precision drug delivery, flotation technology, mineral processing, industrial wastewater treatment, and biomedical imaging.[10,11] The role of persistent bubbles in nanoparticle synthesis produced by ablating solid targets such as Ti, Fe, Al, Cu, Au, and Ag in liquid has already been reported.[4,12] Due to the unique physiochemical properties of the microbubbles, the dynamics of the Mn_2O_3-filled microbubbles are studied here. Laser irradiation of the Mn target immersed in water leads to the formation of Mn_2O_3 nanoparticles and transient bubbles.[13] Amongst other available manganese-based oxides, Mn_2O_3 is the most efficient catalyst for water oxidation.[14] Mn_2O_3 shows multiferroicity and magnetoelectric coupling.[15] Trivalent manganese oxide with Jahn–Teller (J.T.) distortion induces high activity for the oxygen evolution reaction (OER).[16] Known to be an earth-abundant, low-cost material with less toxicity, it acts as an energy harvesting material and finds use in fuel cells, water splitting, supercapacitors, metal–air batteries, rechargeable batteries, and cathode materials in aqueous and non-aqueous batteries.[2,6,17]

Recent trends in sustainable cooling use microfluidics in the thermal management of electronic devices. Thus, the velocity gradients imparted by macro bubbles leading to microstreaming and perturbing the trajectories of microbubbles for electrode deposition of Mn_2O_3 materials are investigated.[18] In this work, external electrodes with D.C. are placed across the laser-irradiated manganese target in water. Electric field-assisted laser ablation in liquids (EFLAL) is used to study its effect on electrode deposition.[19,20]

2. Experimental set-up

In Fig. 1, a target holder is used to hold a manganese target of size 4 mm at the bottom of the liquid cell filled with a distilled-

[a] *Department of Physics, National Institute of Technology Meghalaya, Shillong, 793003, India. E-mail: n.arpita@nitm.ac.in*
[b] *Department of Physics, Pandit Deendayal Energy University, Gandhinagar, 382007, India*
[c] *Department of Physics, Indian Institute of Technology Guwahati, Guwahati, 781039, India*

† Electronic Supplementary Information (ESI) available. See DOI: https://doi.org/10.1039/d3cp05939a

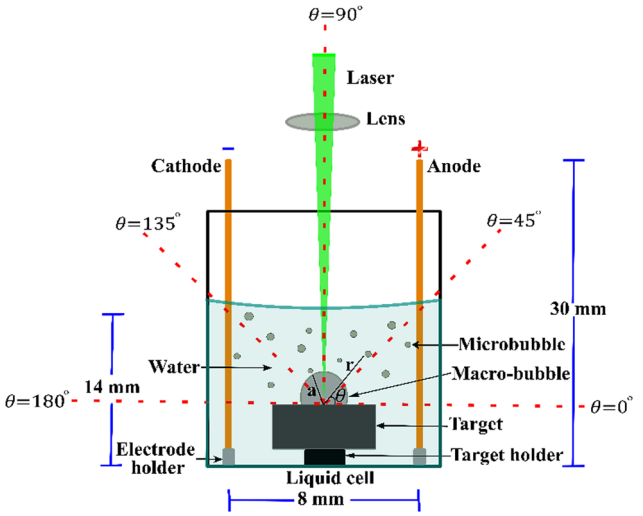

Fig. 1 Electric field-assisted laser ablation in liquid (EFLAL).

deionized water layer up to a height of 14 mm. Two parallel copper electrodes (30 mm × 15 mm), placed inside electrode holders, are kept 8 mm apart with the manganese target at the center and connected to a D.C. power source (Indosaw SE1004) to create an external electric field in the range of 0–3750 V m^{-1}. The target is ablated with a Nd:YAG pulsed laser (Continuum ML II) with a 6 ns pulse duration, 532 nm wavelength (polarisation: vertical), 10 Hz repetition rate, and 25 mJ energy. For ablation, a plano-convex lens (focal length = 10 cm) focuses the laser beam to a spot size of ~229 μm, creating a laser fluence of 61 J cm^{-2}. The ablation of the manganese target creates a plasma followed by a macro bubble at the target–liquid interface and microbubbles in the surrounding liquid. The angular dependence (0–180°) is taken about the center of the macro bubble, as shown in Fig. 1. Following ablation for 15 min, nanoparticles are dispersed in water, and electrode deposition is also observed. The nano-colloidal solution formed after ablation is drop-casted onto a nickel grid for TEM (JEOL JEM-2100) measurements and a cleaned glass slide for micro-Raman spectroscopy (Renishaw inVia Basis) analysis. The electrode depositions are characterized using XRD (Rigaku SmartLab SE), SEM (JOEL JSM-6360), and micro-Raman spectroscopy (Renishaw inVia Basis).

3. Results and discussion

3.1. Nanoparticle characterization

TEM analysis confirms the formation of particles in the nano-range, as shown in Fig. 2, depicting the nanoparticles formed at (a) 0 V m^{-1} and (b) 3750 V m^{-1} applied electric field. The corresponding SAED pattern is shown in the inset of Fig. 2. The circular diffraction rings at 0 V m^{-1} correspond to the (222), (204), (622), (662), and (806) planes of cubic bixbyite α-Mn_2O_3. The three diffraction rings of the sample ablated in the presence of a 3750 V m^{-1} electric field correspond to the (222), (204), and (622) planes of α-Mn_2O_3 nanoparticles.[13,21]

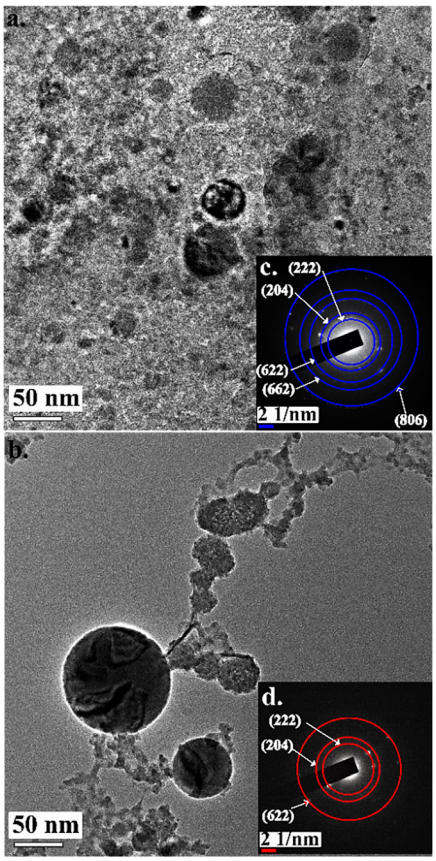

Fig. 2 TEM images of the nanoparticles formed at (a) 0 V m^{-1} and (b) 3750 V m^{-1}. The insets show the SAED patterns of the obtained nanoparticles at (c) 0 V m^{-1} and (d) 3750 V m^{-1}.

The two observed Raman active modes at 545 cm^{-1} and 648 cm^{-1} shown in Fig. 3 are due to the oxygen bridge stretching asymmetrically in Mn–O–Mn and symmetric stretching of the Mn–O bond of Mn^{3+} ions in the octahedral sites, respectively.[22,23] This affirms the formation of cubic bixbyite structured α-Mn_2O_3 ($Ia\bar{3}$) nanoparticles in water.

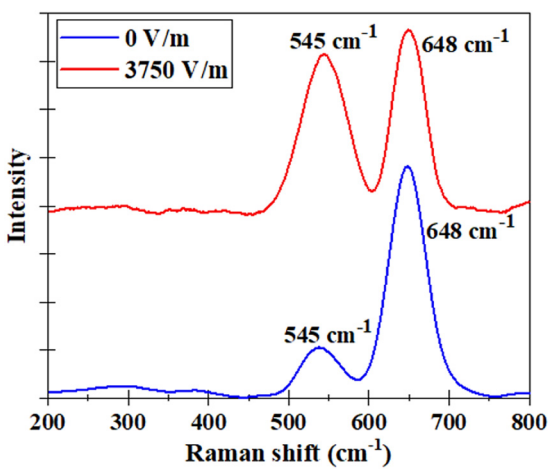

Fig. 3 Micro-Raman spectra of the nanoparticles found in water at 0 V m^{-1} (blue line) and 3750 V m^{-1} (red line) electric field.

3.2. Electrode deposition

Post laser ablation, deposition on "Cu" electrodes is analyzed. The micro-Raman spectra of the electrode at 0 V m^{-1} and 3750 V m^{-1} are shown in Fig. 4(a). Four Raman modes are observed in the absence of the electric field; however, an extra peak at 330 cm^{-1} emerges in the presence of an electric field of 3750 V m^{-1}. The Raman modes at 220 cm^{-1} and 416 cm^{-1} are assigned to the $2E_{\mu}$ and A_{μ} vibrational modes of Cu_2O, respectively.[24] The one at 330 cm^{-1} is due to the $B^{(1)}_{g}$ vibrational modes of CuO.[24,25] The Raman peaks of the Mn_2O_3 nanoparticles deposited on the electrodes have redshifted to 530 cm^{-1} and 626 cm^{-1} peaks. The peaks are assigned to the asymmetric stretching of oxygen bridge species (Mn–O–Mn) and the symmetric stretching mode of Mn^{3+} ions in the Mn–O bond in α-Mn_2O_3 nanoparticles.[22] The substrate (electrode) that collects the Mn_2O_3 nanoparticles is copper which oxidizes in the presence of water.

Fig. 4(b) depicts the XRD pattern of the electrode at 0 V m^{-1} and 3750 V m^{-1} applied electric field. The sharp peaks positioned at 26°, 28° and 34° are assigned to cubic bixbyite α-Mn_2O_3 nanoparticles, which correspond to reflection from the (220), (310), and (222) planes.[26] The other peaks at 269° and 36° correspond to the (110) and (111) planes of Cu_2O, respectively, whereas that at 31° is due to reflection from the (110) plane of CuO.[24] Thus, the deposition of α-Mn_2O_3 on the electrodes is also affirmed.

Conventionally, the pulsed laser deposition in liquids is carried out by keeping the substrate parallel to the target for optimum deposition of target materials.[27] Laser plasma in liquid depicts ~70 times smaller expansion velocities as compared to ambient air with the ion and electron densities mostly confined along the direction of the laser plasma.[28] The ejection of materials from the collapse of transient bubbles (macro) attached to the target is also predominantly directed toward the source laser. In contrast, the electrode deposition here is observed by placing the electrodes orthogonal to the target geometry. Thus, it is intriguing to explore the dynamics of the underwater electrode deposition. To divulge more, the Cu electrode where Mn_2O_3 gets deposited (0°– 45°) is characterized using SEM.

The nanoparticles formed by nanosecond PLAL are said to be negatively charged due to the absorbed electrons onto the nanoparticles synthesized using this technique.[29] Hence, SEM analysis has been carried out on the positively charged electrode. The SEM images of the electrodes, as shown in Fig. 5, at (a) 0 V m^{-1} and (b) 3750 V m^{-1} show the deposition of α-Mn_2O_3 nanoparticles on the "Cu" electrodes. The EDX data (not shown here) reveal an increment in Mn content by 10% with the application of an electric field. Also, in the presence of an

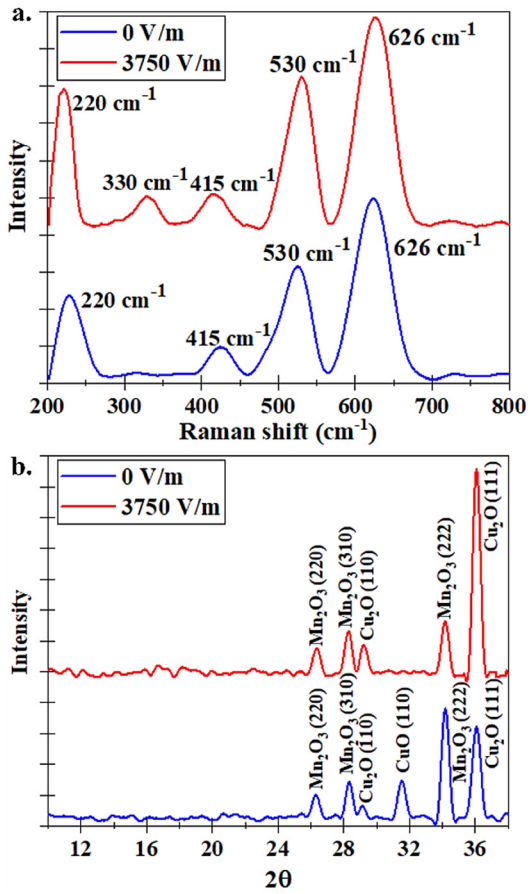

Fig. 4 (a) Micro-Raman spectra of the electrodes without (0 V m^{-1}) and with (3750 V m^{-1}) applied electric field. (b) XRD pattern of the electrodes at an applied electric field of 0 V m^{-1} and 3750 V m^{-1}.

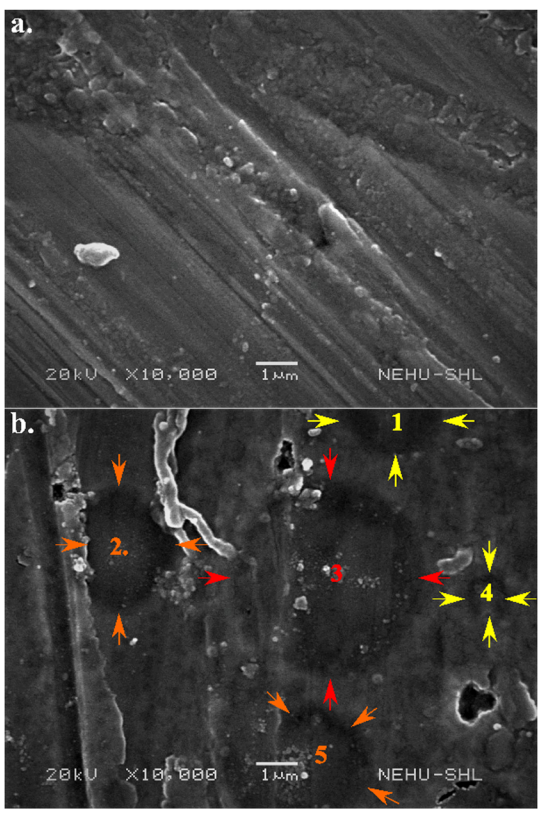

Fig. 5 SEM images showing the surface of electrodes post-ablation at (a) 0 V m^{-1} and (b) 3750 V m^{-1} deposition. To divulge more, the Cu electrode where Mn_2O_3 gets deposited (0°–45°) is characterized using SEM.

external electric field (Fig. 5(b)), micro-sized circular layers of dimension 2–5 μm (arrows marked as 1–5) on the electrodes are visible. These circles are attributed to forceful bombardment by the periphery of micro-sized bubbles onto the electrodes. The dimension of these circular impacts depends on the contact radius.[30] Most microbubbles collapse, disperse nanoparticles in the liquid, or act as nucleation sites, while few get deposited onto the electrodes.

3.3. Streamline motion of microbubbles

The microbubbles in PLAL are also observed using imaging at the target–liquid interface. Fig. 6 shows the shadowgraph image of macro (MB) and micro (Mi-B) bubbles at the target–liquid interface at 0 V m^{-1}. The image is taken after 7 μs of pulsed laser irradiation on a fresh target and water surface. The experimental details of shadowgraphy are reported elsewhere.[31] Here MB represents the macro bubble (dimension: 1000 μm) is attached to the target, while Mi-B represents microbubbles (dimension: 40–190 μm) dispersed in the surrounding liquid. These persistent bubbles are observed if the applied laser fluence is above the threshold.[2] Fig. 7(a) represents the coordinates of these microbubbles taken from shadowgraphy data repeated over 20 laser shots. The angular coordinates "θ" and radial coordinate "r" of microbubbles are defined about the center of the macro bubble with radius "a."

The macro bubble oscillations (growth, collapse, rebound) impart a gradient in the surrounding liquid flow.[32] The oscillations of the macro bubble will create a streaming motion around it due to its non-linear effects which are localized near its wall with a flow pattern based on the mode of its oscillations. Here, one side of the macro-bubble is fixed to the wall (target), and the bubble undergoes volumetric and translational motion.[33] The bubble streaming Reynolds number (Re_s) is[34]

$$Re_s = \varepsilon^2 \sqrt{\left(\frac{\omega a^2}{\vartheta}\right)} \tag{1}$$

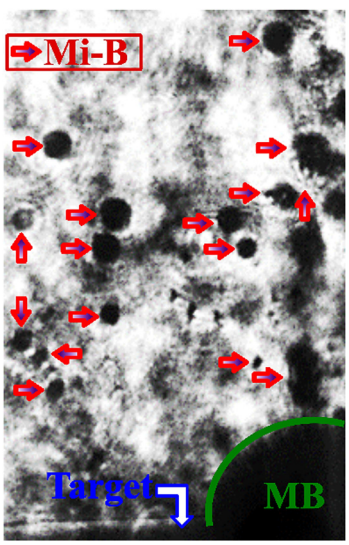

Fig. 6 Shadowgraph image of the target–liquid interface (MB: macro bubble, Mi-B: micro bubble).

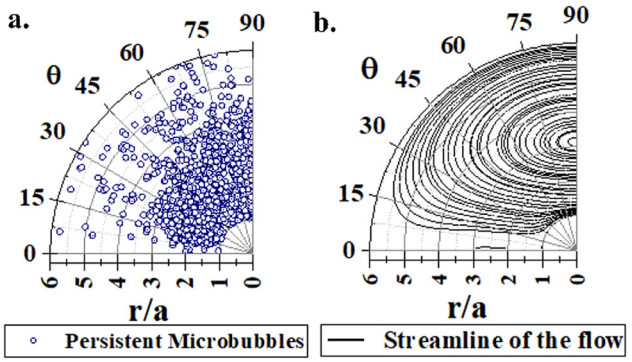

Fig. 7 (a) Coordinates of the microbubble at 0 V m^{-1}. (b) Simulated streamline flow of the microbubbles induced by the oscillations of the macro bubble at 0 V m^{-1}.

where ε, ω and ϑ are the radial oscillation amplitude, frequency of oscillation (2.32 kHz), and kinematic viscosity (1×10^{-5} ms^{-2}), respectively. The value of Re_s is found to be 0.27. Since $Re_s < 1$, Rayleigh–Nyborg–Westervelt (RNW) streaming is considered which is a secondary flow pattern.[34,35] Longuet-Higgins solved the RNW microstreaming (Ψ_2^s) due to the oscillation of a fixed bubble described below:[33]

$$\psi_2^s = \frac{\varepsilon^2}{4} a^3 \omega \sin(\Delta\varphi)\left[-2\frac{r}{a} + \frac{a}{r} + \left(\frac{a}{r}\right)^4\right](\sin\theta)^2 \tag{2}$$

The parameter $\Delta\varphi$ is the phase difference between the volumetric and translational motions of the macro bubble and θ is the flow angle with respect to the horizontal axis along the target surface.

The RNW flow pattern (Ψ_2^s) obtained from eqn (2) is shown in Fig. 7(b). This simulated flow pattern complies with the dispersion pattern of the microbubbles, as shown in Fig. 7(a). For the flow pattern, the higher order contribution in the Navier-Stokes equations is not considered as the shadowgraph image resolution is ~3 μs, and thus the faster transients are not recorded.

3.4. Effect of external electric field on the streamline motion of microbubbles

The influence of the external electric field on the dimension of the macro bubble is reported in the literature.[36] Fig. 8(a) shows the electric field distribution outside the macro bubble. The electric field is given by[37,38]

$$E = \sqrt{E_N^2 + E_T^2} \tag{3}$$

where

$$E_N = E_a \cos\theta\left[1 - \frac{2(k_l - k_v)}{(2k_l + k_v)}\left(\frac{a^3}{r^3}\right)\right] \tag{4}$$

and

$$E_T = -E_a \sin\theta\left[1 + \frac{(k_l - k_v)}{(2k_l + k_v)}\left(\frac{a^3}{r^3}\right)\right] \tag{5}$$

are the normal and tangential electric field components, respectively. E_a, k_l and k_v are the applied electric field and dielectric constants of the liquid and vapor inside the macro

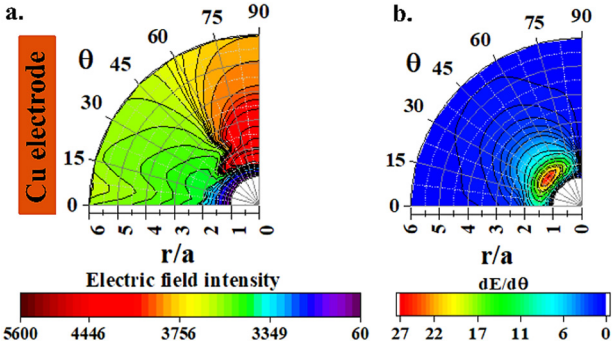

Fig. 8 (a) Electric field intensity outside the macro bubble at 3750 V m^{-1}. (b) An angular gradient of electric field intensity at 3750 V m^{-1}.

bubble, respectively. The angular gradient of the electric field directed away from the wall of the macro bubble is depicted in Fig. 8(b). This indicates that the microbubbles, in addition to microstreaming, experience the electric field gradient directed towards the "Cu" electrode as the nanoparticle-filled bubbles in water exhibit plasma charging.[29] These gradients explain the reason for the higher "Mn" yield and observation of microbubble bombardment onto the "Cu" electrode in the SEM images of Fig. 5(b), explicitly at 3750 V m^{-1}. The effect of the electrostatic double layer (EDL) is not considered here as the laser-assisted phenomena are highly transient and occur at much faster time scales.[13,39] This is experimentally validated by the recent works on electric field-assisted laser ablation in liquids.[37,40]

4. Conclusions

In summary, microbubbles are observed in underwater laser-induced material processing of energy-harvesting Mn_2O_3 nanoparticles. An external electric field is applied to confirm the possible role played by these Mn_2O_3 nanoparticle-filled bubbles for electrode deposition. The external electric field with angular gradients directs the microbubbles onto the electrode. The microbubbles bombard the electrode, exhibiting an enhancement in electrode deposition.

Conflicts of interest

There are no conflicts to declare.

Acknowledgements

The authors sincerely thank the DST-SERB, India (Project File No. ECR/2017/001705) for financial support; DST FIST, India (Project No. SR/FST/PS-I/2019/74) for the financial support for micro-Raman measurements; CIF NIT Meghalaya for carrying out the XRD analysis; and SAIF NEHU Shillong for performing the SEM analysis.

References

1 A. Letzel, M. Santoro, J. Frohleiks, A. R. Ziefuß, S. Reich, A. Plech, E. Fazio, F. Neri, S. Barcikowski and B. Gökce, How the re-irradiation of a single ablation spot affects cavitation bubble dynamics and nanoparticles properties in laser ablation in liquids, *Appl. Surf. Sci.*, 2019, **473**, 828–837.
2 A. Deka, P. K. Baruah, A. Khare and A. Nath, Inquest of material dissipation from cavitation bubble in laser-irradiated solid–liquid interface, *Radiat. Eff. Defects Solids*, 2022, **177**(3–4), 244–257.
3 C. P. Lin and M. W. Kelly, Cavitation and acoustic emission around laser-heated microparticles, *Appl. Phys. Lett.*, 1998, **72**(22), 2800–2802.
4 K. Sasaki and N. Takada, Liquid-phase laser ablation, *Pure Appl. Chem.*, 2010, **vol. 82**(6), 1317–1327.
5 S. Ibrahimkutty, P. Wagener, A. Menzel, A. Plech and S. Barcikowski, Nanoparticle formation in a cavitation bubble after pulsed laser ablation in liquid studied with high time resolution small angle X-ray scattering, *Appl. Phys. Lett.*, 2012, **101**(10), 103104.
6 D. Zhang, B. Ranjan, T. Tanaka and K. Sugioka, Underwater persistent bubble-assisted femtosecond laser ablation for hierarchical micro/nanostructuring, *Int. J. Extreme Manuf.*, 2020, **2**(1), 015001.
7 Y. Li, X. Liu, Q. Huang and T. Arai, Controlled rotation of micro-objects using acoustically driven microbubbles, *Appl. Phys. Lett.*, 2021, **118**(6), 063701.
8 M. R. Kalus, N. Bärsch, R. Streubel, E. Gökce, S. Barcikowski and B. Gökce, How persistent microbubbles shield nanoparticle productivity in laser synthesis of colloids - Quantification of their volume, dwell dynamics, and gas composition, *Phys. Chem. Chem. Phys.*, 2017, **19**(10), 7112–7123.
9 M. R. Kalus, R. Lanyumba, N. Lorenzo-Parodi, M. A. Jochmann, K. Kerpen, U. Hagemann, T. C. Schmidt, S. Barcikowski and B. Gökce, Determining the role of redox-active materials during laser-induced water decomposition, *Phys. Chem. Chem. Phys.*, 2019, **21**(34), 18636–18651.
10 G. Han, S. Chen, S. Su, Y. Huang, B. Liu and H. Sun, A review and perspective on micro and nanobubbles: What They Are and Why They Matter, *Miner. Eng.*, 2022, **189**, 107906.
11 J. D. Dove, M. A. Borden and T. W. Murray, Optically induced resonance of nanoparticle-loaded microbubbles, *Opt. Lett.*, 2014, **39**(13), 3732.
12 M. R. Kalus, S. Barcikowski and B. Gökce, How the Physicochemical Properties of the Bulk Material Affect the Ablation Crater Profile, Mass Balance, and Bubble Dynamics During Single-Pulse, Nanosecond Laser Ablation in Water, *Chem. Eur. J.*, 2021, **27**(19), 5978–5991.
13 S. M. Kharphanbuh, A. Phukan and A. Nath, Magnetic Field Assisted Nucleation dynamics of Laser induced Manganese Oxide nanoparticles in water, *J. Phys. D: Appl. Phys.*, 2022, **55**(37), 375002.
14 A. Ramírez, P. Hillebrand, D. Stellmach, M. M. May, P. Bogdanoff and S. Fiechter, Evaluation of MnO_x, Mn_2O_3, and Mn_3O_4 electrodeposited films for the oxygen evolution reaction of water, *J. Phys. Chem. C*, 2014, **118**(26), 14073–14081.
15 M. Chandra, S. Yadav, R. J. Choudhary, R. Rawat, A. K. Sinha, M. B. Lepetit and K. Singh, Multiferroicity

and magnetoelastic coupling in α- Mn_2O_3: A binary perovskite, *Phys. Rev. B.*, 2018, **92**(10), 104427.
16 J. H. Mokkath, M. Jahan, M. Tanaka, S. Tominaka and J. Henzie, Temperature-dependent electronic structure of bixbyite α- Mn_2O_3 and the importance of a subtle structural change on oxygen electrocatalysis, *Sci. Technol. Adv. Mater.*, 2021, **22**(1), 141–149.
17 K. K. Hazarika, C. Goswami, H. Saikia, B. J. Borah and P. Bharali, Cubic Mn_2O_3 nanoparticles on carbon as bifunctional electrocatalyst for oxygen reduction and oxygen evolution reactions, *Mol. Catal.*, 2018, **451**, 153–160.
18 R. van Erp, R. Soleimanzadeh, L. Nela, G. Kampitsis and E. Matioli, Co-designing electronics with microfluidics for more sustainable cooling, *Nature*, 2020, **585**(7824), 211–216.
19 D. Sapkota, Y. Li, O. R. Musaev, J. M. Wrobel and M. B. Kruger, Effect of electric fields on tin nanoparticles prepared by laser ablation in water, *J. Laser Appl.*, 2017, **29**(1), 012002.
20 G. Compagnini, M. Sinatra, P. Russo, G. C. Messina, O. Puglisi and S. Scalese, Deposition of few layer graphene nanowalls at the electrodes during electric field-assisted laser ablation of carbon in water, *Carbon*, 2012, **50**(6), 2362–2365.
21 E. Moharreri, W. Hines, S. Biswas, D. Perry, J. He, D. Murray-Simmons and S. Suib, Comprehensive Magnetic Study of Nanostructured Mesoporous Manganese Oxide Materials and Implications for Catalytic Behavior, *Chem. Mater.*, 2018, **30**(3), 1164–1177.
22 B. Saha, S. K. Jana, S. Majumder, B. Satpati and S. Banerjee, Selective Growth of Co-electrodeposited Mn_2O_3-Au Spherical Composite Network Towards Enhanced Non-enzymatic Hydrogen Peroxide Sensing, *Electrochim. Acta*, 2015, **174**, 853–863.
23 A. Ginsburg, D. A. Keller, H. N. Barad, K. Rietwyk, Y. Bouhadana, A. Anderson and A. Zaban, One-step synthesis of crystalline Mn_2O_3 thin film by ultrasonic spray pyrolysis, *Thin Solid Films*, 2016, **615**, 261–264.
24 J. Kaur, A. Khanna, R. Kumar and R. Chandra, Growth and characterization of Cu_2O and CuO thin films, *J. Mater. Sci.: Mater. Electron.*, 2022, **33**(20), 16154–16166.
25 D. Prasanth, K. P. Sibin and H. C. Barshilia, Optical properties of sputter deposited nanocrystalline CuO thin films, *Thin Solid Films*, 2019, **673**, 78–85.
26 S. Sharma, P. Chauhan and S. Husain, Structural and optical properties of Mn_2O_3 nanoparticles & its gas sensing applications, *Adv. Mater. Processes*, 2021, **1**(2), 220–225.
27 H. Cui, P. Liu and G. W. Yang, Noble metal nanoparticle patterning deposition using pulsed-laser deposition in liquid for surface-enhanced Raman scattering, *Appl. Phys. Lett.*, 2006, **89**(15), 1531241–1531243.
28 T. T. P. Nguyen, R. Tanabe and Y. Ito, Comparative study of the expansion dynamics of laser-driven plasma and shock wave in in-air and underwater ablation regimes, *Opt. Laser Technol.*, 2018, **100**, 21–26.
29 M. Dell'Aglio and A. De Giacomo, Plasma charging effect on the nanoparticles releasing from the cavitation bubble to the solution during nanosecond Pulsed Laser Ablation in Liquid, *Appl. Surf. Sci.*, 2020, **515**, 146031.
30 J. S. Lum, V. Daeichin, D. F. Kienle, D. K. Schwartz, T. W. Murray and M. A. Borden, Changes in microbubble dynamics upon adhesion to a solid surface, *Appl. Phys. Lett.*, 2020, **116**(12), 1237031–1237035.
31 A. Nath and A. Khare, Transient evolution of multiple bubbles in Laser induced breakdown in water, *Laser Part Beams*, 2011, **29**(1), 1–9.
32 R. Manasseh, *Handbook of Ultrasonics and Sonochemistry*, Springer, Singapore, 2nd edn, 2016, pp. 33–68.
33 P. Marmottant and S. Hilgenfeldt, Controlled vesicle deformation and lysis by single oscillating bubbles, *Nature*, 2003, **423**(6936), 151–153.
34 B. J. Davidson and N. Riley, Cavitation microstreaming, *J. Sound Vib.*, 1971, **15**(2), 217–233.
35 C. Wang, S. V. Jalikop and S. Hilgenfeldt, Size-sensitive sorting of microparticles through control of flow geometry, *Appl. Phys. Lett.*, 2011, **99**(3), 034101.
36 A. Phukan, S. M. Kharphanbuh and A. Nath, An empirical experimental investigation on the effect of an external electric field on the behaviour of laser-induced cavitation bubbles, *Phys. Chem. Chem. Phys.*, 2023, **25**(3), 2477–2485.
37 S. M. Kharphanbuh and A. Nath, Laser-Induced Plasma and Cavitation Bubble Dynamics at Manganese-Water Interface Under External Electric Fields, *IEEE Trans. Plasma Sci.*, 2024, **52**(2), 300–309.
38 M. C. Zaghdoudi and M. Lallemand, Study of the behaviour of a bubble in an electric field: steady shape and local fluid motion, *Int. J. Therm. Sci.*, 2000, **39**(1), 39–52.
39 R. Morrow and D. R. Mckenzie, The time-dependent development of electric-double-layers in pure water at metal electrodes: The effect of an applied voltage on the local pH, *Proc. R. Soc. A*, 2012, **468**, 18–34.
40 H. Mozaffari and M. H. Mahdieh, Enhancement of ablation rate and production of colloidal nanoparticles by irradiation of metals with nanosecond pulsed laser in presence of external electric field, *Phys. Lett. A*, 2019, **383**, 646–654.

